




Modelling of Droplet Capture in an Open-Cell Metal Foam at the Pore and Macroscopic Scales

Thiago P. de Carvalho¹ · David M. Hargreaves¹  · Hervé P. Morvan² · Michael Klingsporn³

Received: 3 May 2022 / Accepted: 18 February 2023
© The Author(s) 2023

Abstract

Open-cell metal foams are often used in applications where particulate and/or droplet capture is important. Here a Computational Fluid Dynamics (CFD) modelling approach is described which models the metal foam at both the pore-scale and the macroscopic scale. At the pore-scale, the detailed internal geometry of the foam is included and the flow field and droplet tracking and capture is modelled explicitly. At this scale, a coefficient is found for each metal foam that relates the distance a droplet can freely travel through the foam to both the droplet diameter and the Darcian velocity in the porous medium. Then, at the macroscopic scale, the coefficient from the pore-scale droplet capture simulations is used in a novel stochastic particle extinction model. Here, the droplets travel through a porous zone and are removed from the model, the probability of which is determined by the coefficient from the pore-scale modelling. A test case is described in which the macroscopic model is verified against the pore-scale model with acceptable levels of accuracy.

Article Highlights

- Single phase CFD and Lagrangian particle tracking are carried out in a range of open-cell metal foams at the pore-scale.
- A capture probability of the droplets as a function of droplet diameter and Reynolds number for each metal foam is found.

✉ David M. Hargreaves
david.hargreaves@nottingham.ac.uk

Thiago P. de Carvalho
tpcarvalho2@gmail.com

Hervé P. Morvan
herve.morvan@rolls-royce.com

Michael Klingsporn
michael.klingsporn@rolls-royce.com

¹ Faculty of Engineering, University of Nottingham, University Park, Nottingham NG7 2RD, UK

² Rolls-Royce plc, Derby, UK

³ Rolls-Royce Deutschland Ltd & Co KG, Dahlewitz, Germany

- The probability of capture is used in a new macroscale droplet capture model, based on Lagrangian particle tracking.

Keywords Droplet capture · Metal foam · Computational fluid dynamics · Lagrangian particle tracking

1 Introduction

Open-cell foams are used in what are sometimes referred to as functional applications such as in heat exchangers, filters, separation devices, catalyst supports, flow distributors and biological implants (Banhart 2001). The high surface area per unit volume and low density make them especially attractive as filters. However, due to the foam's intricate geometry, the acquisition of detailed experimental data can only take place at the macroscopic scale where quantities such as pressure drop can be relatively easily measured, albeit often only for single phase flows.

The assessment of the droplet capture effectiveness within open-cell metal foams is of interest in a number of fields, such as demisters. For example, Ji et al. (2016) looked at the efficiency of a metal foam to collect water from foggy air. A small, cylindrical sample of a copper foam was exposed to an air stream containing water mist and the ability of the metal foam to trap the water was measured experimentally. They confirmed that the device could be made more efficient by rotating the metal foam, encouraging the captured water to migrate radially by the centrifugal force. They mention briefly what appears to be the results of CFD modelling of the droplets as they pass through an isolated metal foam cell. The particles appear to be purely for illustrative purposes because several of them are seen to pass through the ligaments. However, the focus of the paper is more on the water film that forms on the metal foam ligaments and how that moves under the influence of the centrifugal force.

In nanofibrous filters, CFD modelling has been conducted looking at the impaction of sub-micron particle on the individual fibres of these filters (Hosseini and Vahedi Tafreshi 2010a, b). Using both 2D and 3D modelling, they looked to obtain capture efficiency correlations, although the scales and air flow rates are quite different to the present application. Nonetheless, they were able to demonstrate that 3D modelling, in particular, was able to highlight deficiencies in existing correlations, which were applicable at larger scales. It is important to note that at the scales they were modelling, inertial impaction was deemed insignificant, which is not the case in the present work.

At the pore- (or microscopic) scale, researchers are using numerical modelling techniques to gain greater insights into the flow of fluids inside the pore space of the foams. A good example of this approach was that taken by Gerbaux et al. (2010) who compared the results from a number of pore-scale numerical simulations with experimental data for three different metal foams. They describe in detail the construction of the numerical models from microtomography scans of the foams. They found good agreement between experimental and numerical permeability values for all three samples. Based on those ideas, another such study, and a precursor to the present research, involved the Computational Fluid Dynamics (CFD) modelling of the pressure drop across open-cell metal foams at the pore-scale (de Carvalho et al. 2017). A similar approach was adopted by Nie et al. (2018), but they focussed on the pore-scale tracking of oil droplets within the foam, similar to the

approach taken in de Carvalho et al. (2015). Both these studies were able to parameterise the oil capture efficiency for a range of porous media properties. To the knowledge of the authors, however, the step from the capture efficiency at pore-scale to an analogous implementation in macroscopic CFD models was not made and this paper serves to address that omission. In much the same way as pore-scale models can be used to determine permeability values that then can be used in porous zone models at macroscale (e.g. CFD models with embedded porous sub-domains), this paper outlines how the pore-scale capture efficiency can be used in a macroscopic model using a novel droplet capture algorithm. The idea is a simple but compelling one: as droplets move through the porous region, their probability of capture increases the longer they are in the region. This capture probability is related to the capture efficiency from the pore-scale model. The process is a stochastic one, meaning that some particles may traverse the porous region, while some may not. Details can be found in Sect. 3. It should be stated that this method currently only applies and is implemented for Finite Volume CFD models. The ultimate application of this work is the separation of oil droplets from a high speed air stream. In fact, this work is part of an ongoing project which aims to develop a numerical modelling framework for an aero-engine air/oil separator. Oil enters the device in the form of dispersed droplets and primary separation takes place by centrifuging larger droplets, with secondary separation occurring as smaller droplets are coalesced within an open-cell metal foam (de Carvalho et al. 2016). The choice of boundary conditions and material properties, therefore, are determined with this application in mind.

The remainder of the paper is organised as follows. The paper is broadly divided into two parts: Sect. 2 describes the air flow and droplet capture modelling at the pore-scale. That is, where the actual, cell-by-cell structure of the metal foam is considered. Then, Sect. 3 sets out the new model that takes the pore-scale particle tracking results and implements them in a macroscopic model. Finally, Sect. 4 summarises the new macroscopic droplet capture model and suggests future avenues of numerical and experiment work to validate it further.

2 Modelling at the Pore-Scale

2.1 Modelling the Air Flow

Although it was described in detail in de Carvalho et al. (2017), it is useful to describe comparatively briefly the approach taken to producing flow simulations at the pore-scale using CFD. In all, five different commercially available foams were investigated: a Recemat nickel-chromium 17 to 23 PPI (Pores Per Inch), two Retimet[®] nickel foams with 45 and 80 PPI and two Alantum[®] Inconel 625 alloy foams, one with a nominal pore size of 450 μm and a hybrid sample with two layers of different pore sizes merged together, namely 580 μm and 1200 μm . Figure 1 shows images obtained using a scanning electron microscope of the Inconel 625 alloy 450 μm foam and a pure nickel foam, similar to the Recemat foam. The web-like solid matrix, made up of many struts (or ligaments) surrounded by an interconnected pore space is clearly seen—this is typical of open-cell foams. The geometric properties of the foams that are studied in this paper are detailed in Table 1 of de Carvalho et al. (2017).

A tomographic dataset comprising of a stack of N_z greyscale images of $N_x \times N_y$ pixels was produced using high-resolution X-ray micro-CT scanning. The pore space and solid

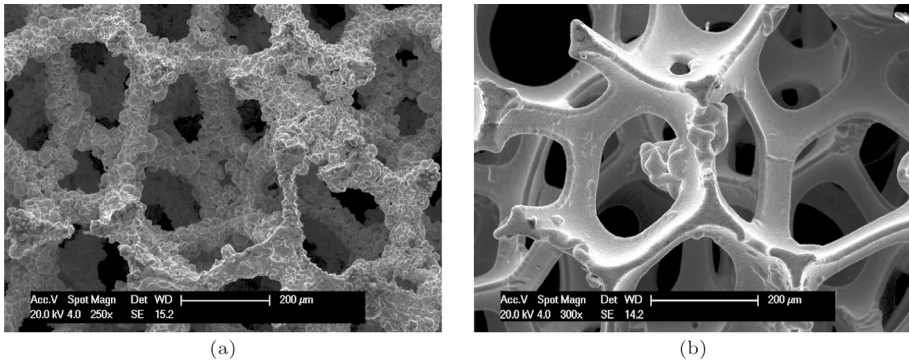


Fig. 1 Scanning electron microscope images of **a** Inconel 625 alloy 450 μm foam and **b** pure nickel 450 μm foam (de Carvalho et al. 2017)

parts of the porous media have distinct optical densities. Some complex image processing of the greyscale images was required to produce a binary image, such as that shown in Fig. 2a. An added complication was the fact that some of the ligaments were hollow, presenting the image processing with a particularly difficult problem. Nevertheless it was possible, using a marching cubes algorithm to generate a triangulated representation of the pore-solid interface, which was then converted into a stereo-lithography format (STL), a image of which is shown in Fig. 1b.

The STL file was read into the meshing software of the ANSYS suite of software, was cleaned up and ultimately sliced to make a cuboid sample, which corresponded geometrically to the experimental samples of Oun and Kennedy (2014). This experimental data were used for validation of the CFD modelling and the results are published in de Carvalho et al. (2017). A polyhedral mesh was generated throughout the domain and Fig. 3a shows the surface mesh on a number of ligaments, while Fig. 3b shows a 2D slice through the mesh. For completeness, the domain and boundary conditions used for the single-phase

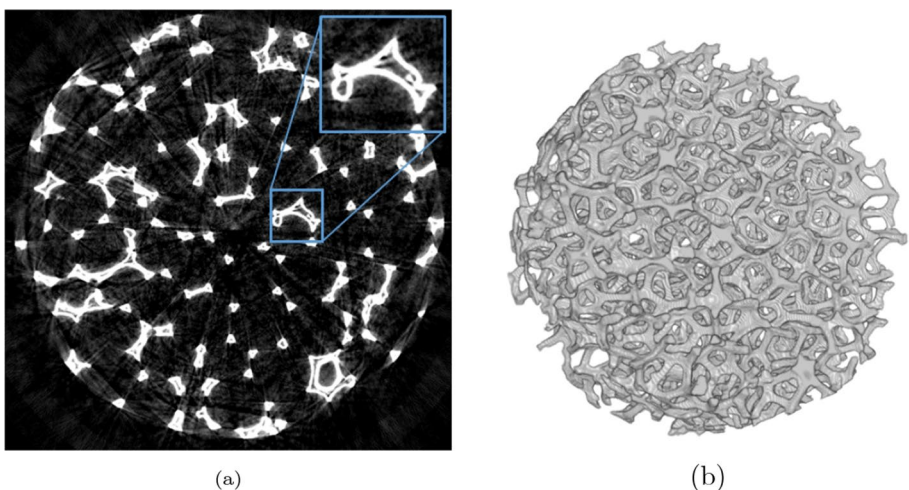


Fig. 2 **a** 2D cross-sectional reconstruction of the Recemat foam geometry, highlighting a hollow strut; **b** 3D rendering of the a 12 mm diameter cylindrical Recemat sample (de Carvalho et al. 2017)

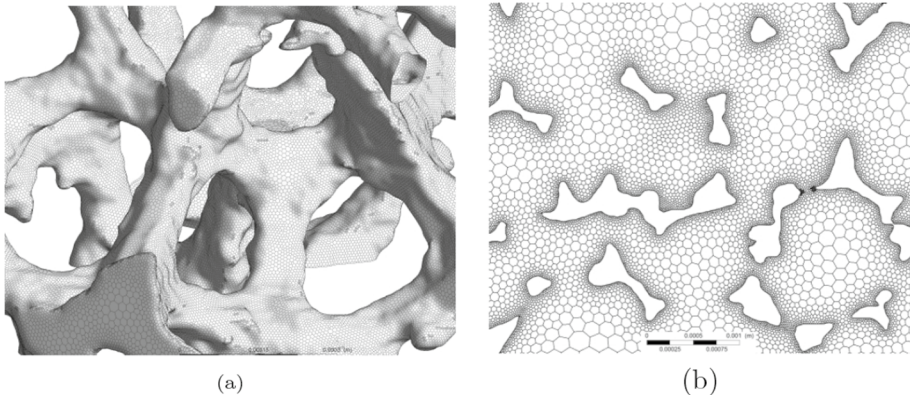


Fig. 3 View of the **a** surface polyhedral mesh and **b** sectional view of the pore space mesh (de Carvalho et al. 2017)

air flow modelling are shown in Fig. 4. Steady-state turbulent Reynolds-Averaged (RANS) models were used throughout the study with the inlet velocity, u_D , being varied for each of the five metal foams. In each case, the pressure drop, Δp , across the sample was calculated and compared against the experimental data, showing good agreement throughout.

The goal of the pore-scale air flow modelling was to produce Forchheimer coefficients, F for use in macroscale models of the porous media,

$$\frac{\Delta p}{L_f} = -\frac{\mu}{K}u_D - F\rho u_D^2 \tag{1}$$

where L_f is the length of the porous media in the streamwise direction, μ is the dynamics viscosity of air, ρ is the density of air and K is the permeability. The Forchheimer

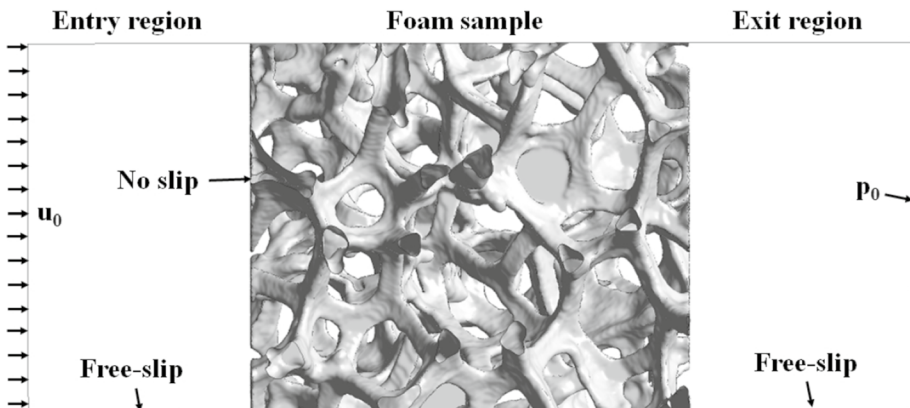


Fig. 4 Schematic of the computational domain and boundary conditions (de Carvalho et al. 2017)

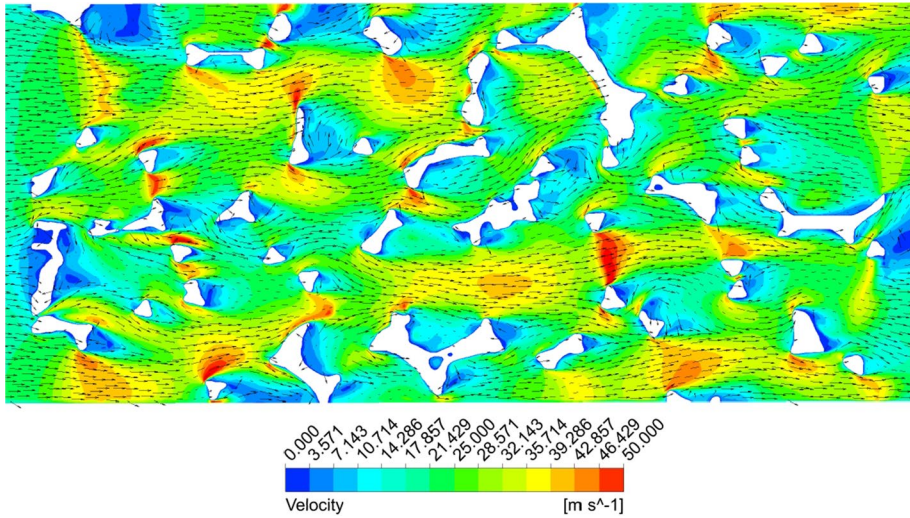


Fig. 5 Superimposed contour and vector plots of the velocity magnitude and vector on a 2D cut plane parallel to the flow direction located at the centre of the domain with $u_D = 20 \text{ m/s}$ (de Carvalho et al. 2017)

coefficient, F , which is believed to be fixed for a given class of porous media (Dukhan et al. 2014). The first term in Eq. 1 is the Darcy term, which accounts for viscous losses through the porous media. de Carvalho et al. (2017) were able to show that the form drag term (the Forchheimer term) was far greater than the Darcy term, due to the open structure of the metal foams.

In a macroscale model, the microscopic representation of the metal foam is replaced by a region in space in which a momentum sink is applied to the governing flow equations, mimicking the effect of porous region. In this way, the pressure drop due to the presence of the porous media can be modelled without resorting to meshing the detailed internals of the porous region. When we discuss the particle tracking methodology of Sect. 3, a similar approach will be taken: producing a macroscopic representation of the particle capture process from a series of pore-scale (or microscopic) simulations.

In light of this, the air flow within the metal foams is of key importance in the present work on droplet capture. Figure 5 shows both contours of velocity magnitude and velocity vectors for one of the cases studied in de Carvalho et al. (2017). Areas of high speed flow (indicated by the yellow and red contours) can be seen as the flow accelerates through the windows between adjacent cells of the foam.

2.2 Standard Lagrangian Tracking Formulation

The numerical modelling of gas-liquid two-phase flow in a Computational Fluid Dynamics (CFD) framework can be divided into Eulerian-Eulerian and Eulerian-Lagrangian approaches. Eulerian-Eulerian methods solve both phases in the same inertial frame of reference, and some models also require an additional interface tracking algorithm. The volume of fluid (VOF) method by Hirt and Nichols (1981) is one example of such type of approach. VOF is suited to model immiscible fluid phases and has extremely stringent mesh requirements in

order to accurately resolve the gas-liquid interface. VOF tends to become very computationally intensive if there is a very high number of liquid droplets and/or ligaments in the flow due to associated mesh size requirements. It performs best when there is a distinct interface between a small number of regions of different phases and is not appropriate for large numbers of particulates or bubbles dispersed in the primary, continuous phase. For such dispersed systems, other Eulerian-Eulerian methods can be used and require empirical relationships such as drag and mass transfer to account for the effect of the disperse phase on the continuous one and vice versa. Again, the volume of fraction is used but is used to represent what proportion of a cell is occupied by the particulate phase.

For dispersed systems, an alternative is to employ an Eulerian-Lagrangian approach to model low volume loading gas-liquid flows. The gas phase is treated as a continuous phase in an Eulerian frame, whereas the droplets (or parcels representative of a certain number of droplets) are treated in a Lagrangian framework, with each droplet having its own reference frame and trajectory. The interaction with the gas phase could cause deformation on the droplet shape due to aerodynamic drag, for example. However, the focus here is on the motion of droplets with small diameters ($< 15 \mu\text{m}$), therefore shape deformation has been deemed negligible. Including other physical models, such as heat and mass transfer, is also implementable in these Eulerian-Lagrangian models.

In the commercial CFD software employed here, ANSYS Fluent, the Lagrangian model is referred to as the Discrete Phase Model (DPM). Numerically, each representative droplet is essentially a mathematical point that travels along the continuous phase, with an associated diameter and physical properties. A particle tracking algorithm is employed to solve the Lagrangian phase equations. The DPM approach is able to calculate the motion of a large number of representative droplets using relatively low computational resources. One of the drawbacks is that whenever a droplet comes into contact with a solid surface, a film or another droplet, the resulting absorption or generation of daughter droplets often requires the use of empirical correlations, which are available only for simple idealized cases. However, the work of Peduto et al. (2011) is extending these correlations with high resolution VOF modelling and experimental work. They are, in particular, looking at the impact of oil droplets in films of oil.

In the remainder of this section, the standard Lagrangian particle tracking algorithm in ANSYS Fluent is described for completeness. Within this framework, the fluid phase is treated as a continuum phase by solving the usual Navier-Stokes governing equations. The dispersed phase is solved by tracking a large number of particles through the computed flow field. The particles can be either solid or liquid. The trajectory of a particle is computed by integrating the force balance as

$$\frac{\partial \mathbf{u}_d}{\partial t} = \frac{\mathbf{u}_g - \mathbf{u}_d}{\tau_r} + \frac{(\rho_d - \rho_g)}{\rho_d} \mathbf{g} + \mathbf{F}, \quad (2)$$

where the subscripts g and d refer to the gas and droplet phases, respectively. \mathbf{u} is the velocity, ρ is the density, \mathbf{g} is the gravitational acceleration and \mathbf{F} is an additional acceleration (force/unit droplet mass) term. The second term on the right-hand side is the drag force per unit droplet mass with τ_r defined as the droplet relaxation time

$$\tau_r = \frac{\rho_d d_d^2}{18\mu_g} \frac{24}{C_D \text{Re}_d}, \quad (3)$$

where Re_d is the droplet Reynolds number,

$$\text{Re}_d = \frac{\rho_g d_d |\mathbf{u}_d - \mathbf{u}_g|}{\mu_g}, \quad (4)$$

where μ_g is the dynamic viscosity of the gas phase. Here, the droplets are assumed to be perfectly spherical and non-deforming. The drag coefficient, C_D , is

$$C_D = a_1 + \frac{a_2}{\text{Re}_d} + \frac{a_3}{\text{Re}_d^2}, \quad (5)$$

where a_1 , a_2 and a_3 are constants that apply over several ranges of the particle Reynolds number, and are given in Morsi and Alexander (1972). The droplets are assumed to be inert and hence there is no energy or mass transfer.

The droplet trajectory equation and any auxiliary equations are solved by stepwise integration over discrete time steps. The droplet displacement is computed using a trapezoidal implicit scheme,

$$\mathbf{x}_i^n = \mathbf{x}_i^o + \frac{1}{2} \Delta t (\mathbf{u}_{di}^o + \mathbf{u}_{di}^n), \quad (6)$$

where the subscripts o and n refer to old and new values, respectively, and \mathbf{u}_{di} is the velocity vector of the i th droplet.

The dispersion of droplets due to turbulence in the gas phase is predicted by using a stochastic tracking approach. The random walk model is employed, where the instantaneous velocity fluctuations on droplet trajectories are represented by stochastic methods.

The prediction of turbulent dispersion is achieved by integrating the trajectory equations for individual droplets using the instantaneous fluid velocity, $\bar{u}_d + u'_d(t)$, along the droplet path. The random effects of turbulence are included by computing the trajectories in this manner for a sufficient number of representative droplets.

The discrete random walk (DRW) model simulates the interaction of a droplet with a succession of discrete stylized fluid phase turbulent eddies. The fluctuating velocity components are defined as discrete piecewise functions of time. The interval of time in which their random value is kept constant is defined by the characteristic lifetime of the eddies. Each eddy is characterized by a Gaussian distributed random velocity fluctuation, u' , v' and w' , and a timescale, τ_e . The values of the random velocity fluctuation components that prevail during the lifetime of a turbulent eddy are sampled assuming they obey a Gaussian probability distribution,

$$u' = \zeta \sqrt{u'^2}, \quad (7)$$

where ζ is normally distributed random number and the remainder of the right-hand side accounts for the local root-mean-square (RMS) velocity fluctuations. Assuming the kinetic energy of turbulence is isotropic in the flow, the values of the RMS fluctuating components can be defined as

$$\sqrt{u'^2} = \sqrt{v'^2} = \sqrt{w'^2} = \sqrt{\frac{2k}{3}}, \quad (8)$$

where k is the turbulent kinetic energy. This is valid for the k - ϵ , the k - ω models and their variants. The characteristic lifetime of an eddy is defined as a constant, such as

$$\tau_e = 2T_L, \quad (9)$$

with $T_L \approx C_L \frac{k}{\epsilon}$, where T_L is the integral time, k and ϵ are the turbulent kinetic energy and dissipation rate, respectively, and C_L is a constant that depends on the turbulence model. The characteristic lifetime of an eddy can also be defined as a random variation about T_L , such as

$$\tau_e = -T_L \ln(\lambda), \quad (10)$$

where λ is a uniform random number greater than zero and less than 1. The droplet eddy crossing time is defined as

$$t_{\text{cross}} = -\tau_r \ln \left[1 - \left(\frac{L_e}{\tau_r |\mathbf{u}_g - \mathbf{u}_d|} \right) \right] \quad (11)$$

where L_e is the eddy length scale, τ_r is the droplet relaxation time and $|\mathbf{u}_g - \mathbf{u}_d|$ is the magnitude of the relative velocity.

The droplet is assumed to interact with the continuous phase eddy over the smallest of the eddy lifetime and crossing time. After this time is reached, a new value of the instantaneous velocity is computed by applying a new value of ζ . Thus, the only inputs the DRW model require are the value of the constant C_L , and the choice of eddy lifetime prediction method.

2.3 Simplifications, Assumptions and Boundary Conditions

Nearly every numerical model involves a certain number of simplifications and assumptions due to unknown physics (lack of information regarding initial or boundary conditions) and time constraints due to available computational effort. Some knowledge concerning the form and behaviour of the droplet phase next to the metal foam region is necessary in order to make the right assumptions and develop a suitable CFD approach.

There is no experimental data available concerning the oil flow within open-cell metal foams. The scarcity of information regarding the oil phase poses a problem in the development of an appropriate numerical approach. Willenborg et al. (2008) have measured performed measurements in an aero-engine separator which employed a Retimet 45 PPI foam. The results have shown the presence of sub-micron droplets ($\sim 0.5 \mu\text{m}$) at the separator outlet, thus not being captured by the metal foam. However, it was not possible to measure the droplet diameter distribution at the foam entrance region.

In the present work, it is assumed that the mass fraction of oil at the metal foam inlet should be less than 2%. So, a conservative oil mass fraction of 5 % is assumed at the metal foam entrance for all DPM simulations. No droplet diameter distribution is assumed, instead, separate uniform sized droplet calculations are performed for six diameters ranging from 0.1 to 10 μm . This way, the oil separation effectiveness can be evaluated qualitatively for each individual droplet diameter. This choice of diameter range is quite arbitrary, however, the limited literature points that this diameter range is the most problematic in terms of oil separation for the present application.

The modelling of all physical effects related to droplet dynamics can be very computationally intensive even for a single droplet (Peduto et al. 2011). Droplet deformation and breakup are not taken into account in the present work, which is reasonable given the small droplet sizes being analysed. No dynamic interaction with the metal foam solid structure is considered, such as film formation, splashing, rebounding or stripping. Even though liquid

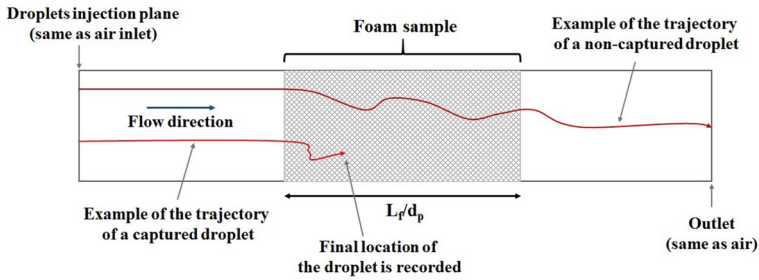


Fig. 6 Schematic of the oil droplet capture criterion

film models are available in ANSYS Fluent, they have a limited range of applicability. The complexity of the solid structure of the foams and the small length scales involved here are likely render such models ill-suited for the present study.

A simplified oil capture criterion is employed, assuming the droplet trajectory to be terminated if it hits the solid structure of the foam. It is assumed that the droplet always sticks to the foam surface if it comes in contact with it. Even though this approach might not be realistic in a sense that all the droplet-solid interaction phenomena is being neglected, it offers a simple way to qualitatively evaluate the separation effectiveness. However, it should be noted that in reality, it is likely that the oil accumulates and forms a film on the surface of the foam. Figure 6 shows a schematic of the oil capture approach employed here, illustrating examples of the trajectories of a non-captured and captured droplet, respectively.

Gasoil-liquid ($C_{16}H_{29}$) was used as the material for the oil phase. An inlet oil mass fraction of 5% results in a volume fraction of approximately 0.008%, which is an important parameter in order to estimate the interaction between the gas and oil phase. According to Eaton (2009), the dispersed phase can have a very strong effect on the gas-phase flow, even at particle volume fractions below 0.1%. Alternatively, Elghobashi (1994) argues that interaction between the gas flow and disperse phase can take place between volume fractions from 0.0001 to 0.1%, with particle-particle interactions being negligible. The oil volume fractions values considered here are within an intermediate range where interaction with the continuous phase may become important. Taking into account the interaction with the gas phase implies the need of a transient simulation, which could raise the computational costs by more than one order of magnitude, compared to a steady-state Lagrangian approach. However, Kulick et al. (1994) showed by means of experiments that the interaction between small dense particles and airflow has mainly attenuated the fluid turbulence, whereas the fluid velocity profiles remained virtually unchanged. In view of these results, and to reduce computational costs, it was decided to not take into account the effect of the droplets on the gas phase. Furthermore, droplet-droplet interactions are neglected.

All Lagrangian calculations are therefore performed as one-way coupled, using the steady-state, converged pore-scale solutions of the airflow. Essentially, the particle tracking is conducted as a post-processing exercise where the particles are injected into the air flow such as that shown in Fig. 5. The results obtained using square channel computational domains are employed. The effect of the airflow velocity on the droplet capture is evaluated by performing the Lagrangian simulations under different airflow velocities, ranging from 5 to 50 m/s. The droplets are injected from a plane located at the air inlet. The particles are injected at the same velocity as the incoming airflow. The droplet dispersion due to

turbulence is taken into account by the use of a random walk stochastic model, detailed in Sect. 2.2.

Since converting the oil injection mass flow rate into the actual number of droplets often results in a prohibitively high number, the concept of a droplet parcel is employed. A parcel can be seen as a representative droplet, with a specified diameter and a relaxation time associated with a single droplet. Therefore, the DPM model actually tracks a number of parcels, each being representative of a certain real number of droplets, and containing a fraction of the total mass flow injected. A sensitivity analysis showed that a total number of 25 000 droplet parcels can produce statistically representative oil capture results that are independent of the number of injected parcels. In this sensitivity analysis, the number of parcels was gradually increased until the proportion captured no longer changed with the number of parcels injected. For each number injected, several runs were conducted to ensure that the stochastic nature of the tracking did not materially change the proportion captured from one simulation to the next. The gravitational force is neglected due to the small droplet mass and relatively large inertial forces.

2.4 Oil Capture Results

The oil capture criterion assumes the termination of the droplet parcel trajectory if it impacts on a wall of the ligaments of the foam surface. As part of this project, the impact of droplets on a ligament with a thin film were modelled using the approach detailed in Kakimpa et al. (2016). However, this is not representative of the metal foam as a whole and could not be implemented here. Therefore, the main separation mechanism here is the droplet's inertia and the only force acting on the droplets is the aerodynamic drag. The streamlines diverge as they approach the metal foam ligaments, since the air passes around the foam solid ligaments. In the case of droplets, if they have sufficient inertia, they tend to follow different trajectories from the fluid streamlines. Typically, the more inertia the droplet has, the larger the deviation from the fluid streamlines, therefore, if the amount of deviation from the fluid streamlines is large enough, the droplet may end up intersecting the solid ligaments and get captured. The diameter of the ligaments here is roughly more than 10 times the size of the largest droplet diameter investigated. Figure 7 illustrates the oil droplet trajectories across the Retimet 45 PPI foam for an inlet velocity of 20 m/s and three different droplet diameters: 0.5, 1 and 3 μm . Clearly, as the droplet diameter increases, so does the number of droplets captured as they pass through the metal foam, since larger droplets have more inertia.

The fraction of escaped (or free) droplets, η_{fd} , is defined as the number of non-captured droplets divided by the total number of droplets injected. In order to determine when a droplet has hit the foam, the full trajectory data is exported from ANSYS Fluent and read by a MATLAB script, which computes the final streamwise position, z , of all droplet trajectories, and then normalizes it by the mean pore size, d_p , of the given foam sample. Thus, the fraction of non-captured droplets is computed at discrete points along the entire length of the foam, generating distinct oil capture curves for each droplet diameter and flow velocity. For example, Fig. 8 shows the oil capture curves obtained with the DPM simulations performed on the Retimet 45 PPI foam at Darcian (or bulk) velocities of 5, 10, 20, 30, 40 and 50 m/s and six different droplet diameters.

These results show, for this case, that the flow velocity has a significant impact on the oil capture for intermediate diameters of 0.5–3 μm . Higher droplet inertia means that the larger particles do not follow the flow streamlines as the flow separates around the

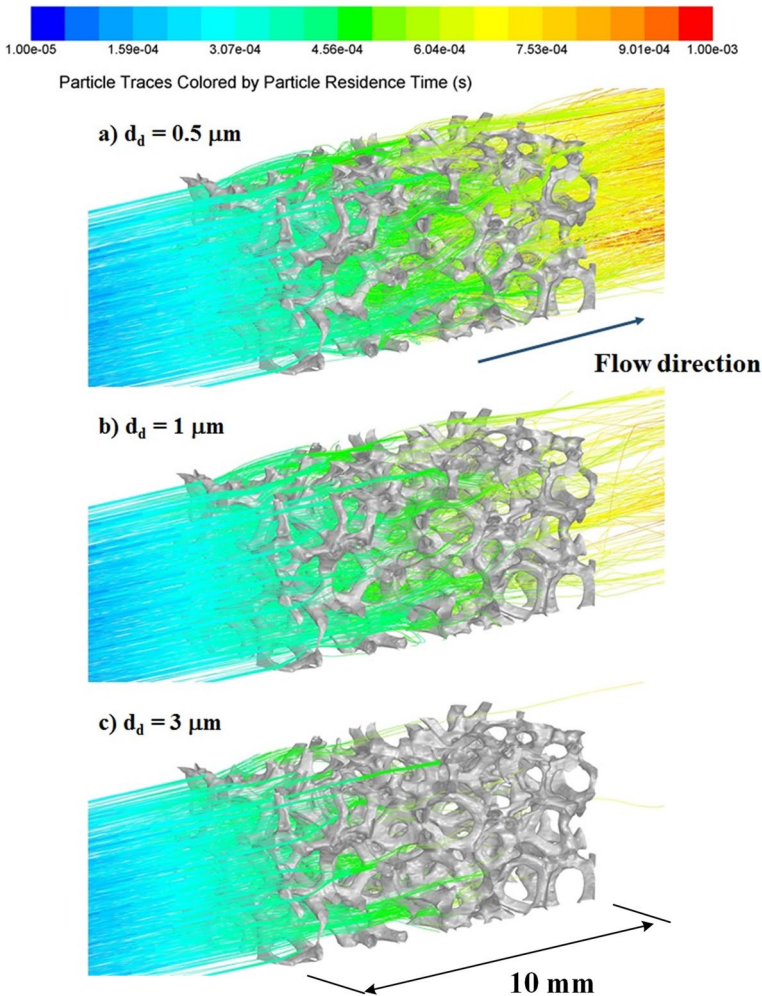


Fig. 7 Droplet trajectories through the Retimet 45 PPI foam for an inlet velocity of 20 m/s and three uniform droplet diameters: **a** 0.5, **b** 1 and **c** 3 μm . The number of trajectories has been reduced for clarity and are coloured by droplet residence time

ligaments, thus leading to a higher probability of collision against the ligaments. A marginal increase in the oil capture is observed for larger droplet diameters (5 and 10 μm) when the flow velocity is increased, since the oil capture is already very high even at low flow velocities. Conversely, for the smallest diameter of 0.1 μm , no clear pattern seems to emerge, and the majority of droplets tend to pass through the foam, with the fraction of free droplets seeming to be independent of the flow velocity.

Oil capture results obtained for the other foams showed a very similar pattern, but with different values of oil capture depending on the foam. Perhaps unsurprisingly, foams with a smaller pore size and larger specific surface area generally showed an increased oil capture when compared with foams with larger pore sizes and smaller specific surface area. In order to quantify this, the fraction of free droplets computed at the

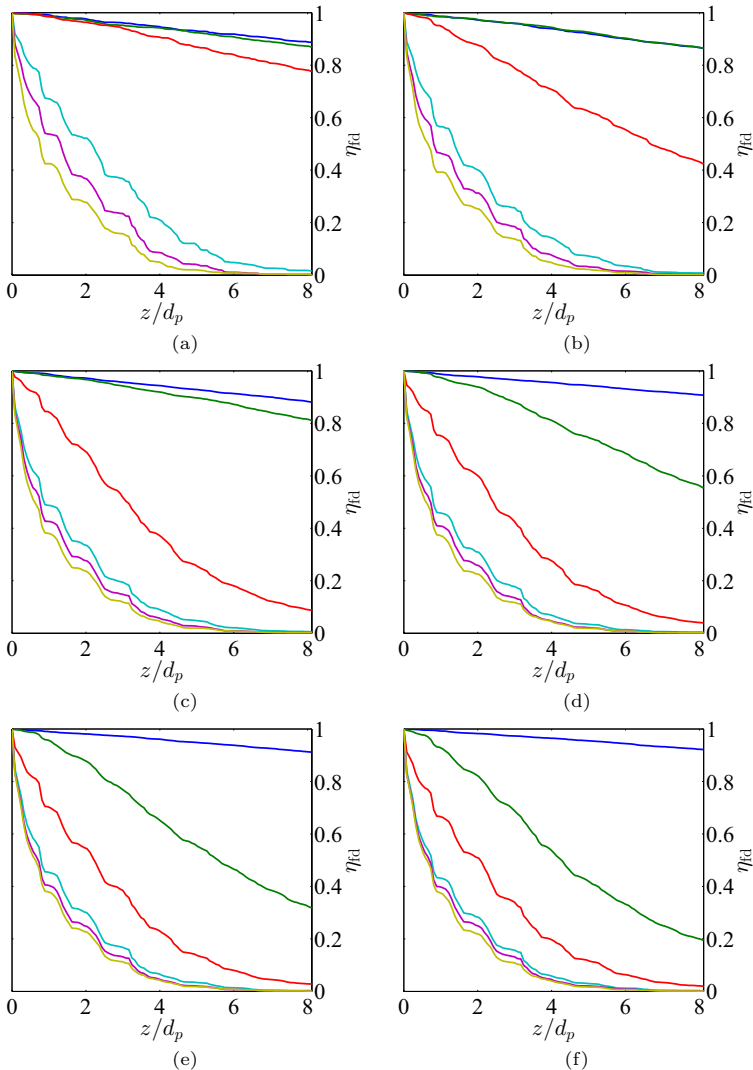


Fig. 8 Lagrangian simulations results showing oil capture curves for the Retimet 45 PPI for different droplet diameters. Results are shown for six Darcian velocities: **a** 5, **b** 10, **c** 20, **d** 30, **e** 40 and **f** 50 m/s. Blue is 0.1 μm , green is 0.5 μm , red is 1 μm , cyan is 3 μm , magenta is 5 μm and yellow is 10 μm

normalized position of $z/d_p = 5$ (roughly five cells into the foam) is plotted together in Fig. 9. For the four different droplet diameters, 0.5, 1, 3 and 5 μm , results show the fraction of free droplets at $z/d_p = 5$ decreases with an increase in the flow velocity for all samples, with this effect being more significant for smaller droplet diameters.

A closer inspection in the results displayed in Fig. 9 show some interesting insights. The Inconel 450 μm sample yielded the highest oil capture, as expected. However, it does so at the expense of having a higher pressure gradient across the sample. The hybrid Inconel (1200 + 580 μm), which has the second highest pressure gradient,

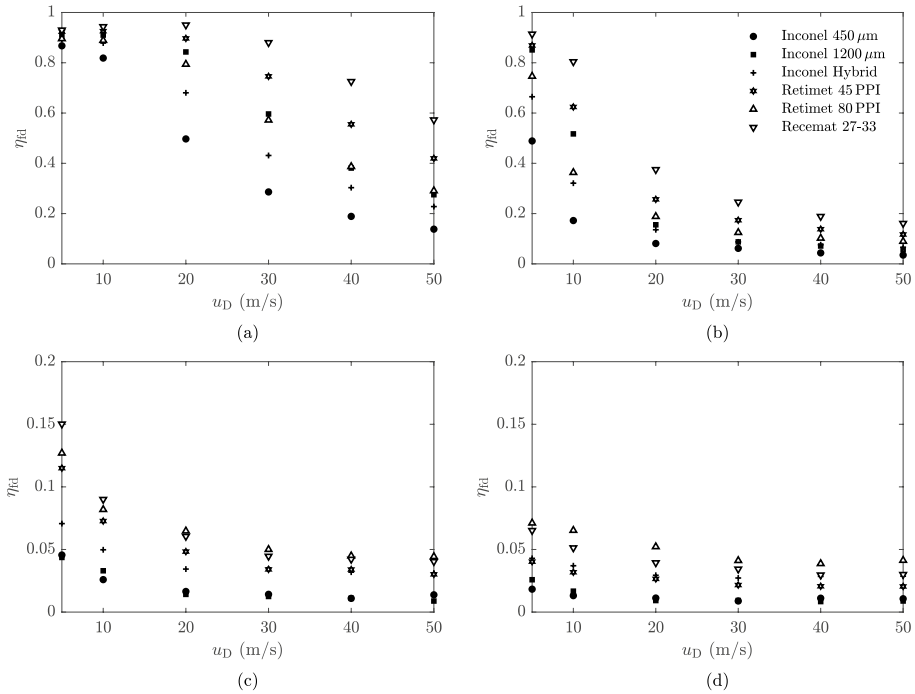


Fig. 9 Fraction of non-captured droplets computed at the normalized position $z/d_p = 5$ versus the Darcian velocity for four different droplet diameters, **a** 0.5, **b** 1, **c** 3 and **d** 5 μm

showed also the second highest oil capture results for droplet diameters of 0.5 and 1 μm . Interestingly, this trend is not observed for droplet diameters of 3 and 5 μm . For these two larger diameters, the Inconel 1200 μm sample showed a better oil capture than the Inconel 1200 + 580 μm foam. This is a largely unexpected result, since the Inconel 1200 μm sample has a smaller specific surface area. The Retimet 80 PPI showed a particularly low oil capture, even lower than the Recemat capture results for diameters of 3 and 5 μm which was quite surprising given that the Recemat has a much larger pore size.

de Carvalho et al. (2017) found that the pressure gradient of the foams is roughly proportional to their specific surface area. Specific surface area is the solid-pore interface area per unit volume and hence has units of m^{-1} . Oil capture was also expected to be roughly proportional to the specific surface area, since a larger value of surface area normally implies a greater number of foam solid ligaments per unit volume, therefore increasing the chances of droplet impact. Figure 10 shows the fraction of non-captured droplets at $z/d_p = 5$, plotted as a function of the specific surface area, under different flow velocities and for four droplet diameters: 0.5, 1, 3 and 5 μm . The fraction of free droplets computed for droplet diameters of 0.5 and 1 μm showed to be inversely proportional to the surface area. However, for larger diameters, no clear trend can be seen, with the Retimet 80 PPI showing the poorest droplet capture relative to its specific surface area. These results seem to imply that the likelihood of a droplet being intercepted by a foam ligament is not only a function of the specific surface area, but also of the particular morphology of the foam solid matrix. Further, the morphology may also be

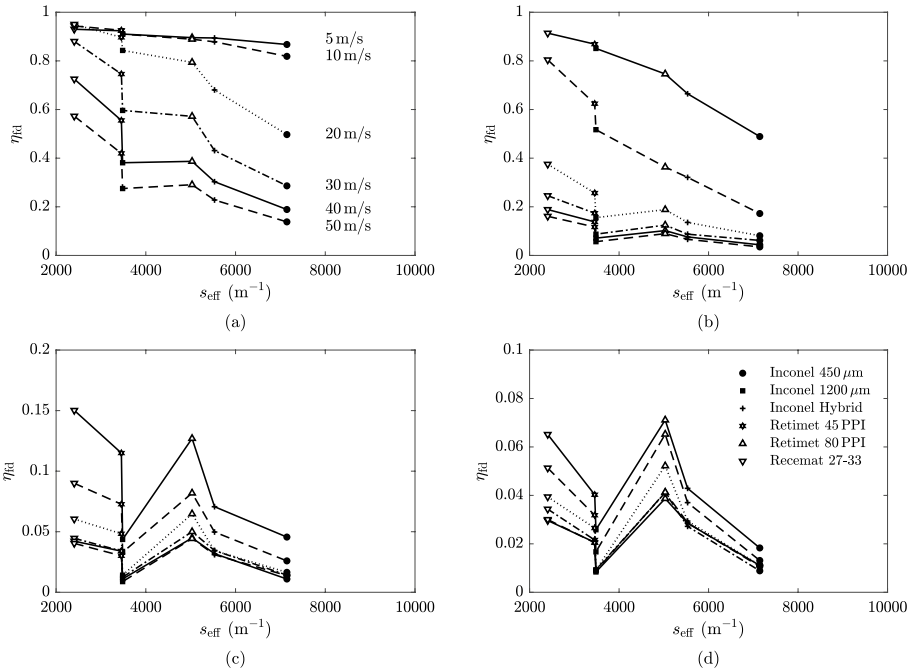


Fig. 10 Fraction of non-captured droplets computed at the normalized position $z/d_p = 5$ versus the specific surface for four different droplet diameters, **a** 0.5, **b** 1, **c** 3 and **d** 5 μm and the five air speeds shown in plot **(a)**

responsible for different levels of daughter droplets created as the droplets impact on the ligaments.

The behaviour of particles in a flow can be described by the dimensionless Stokes number, which is defined as the ratio of the characteristic particle (or droplet) time, t_d , to the characteristic time of the flow, t_f , as

$$\text{Stk} \equiv \frac{t_d}{t_f}. \tag{12}$$

A droplet with a low Stokes number tends to follow the flow streamlines whereas a droplet with a high Stokes number is dominated by inertia and tends to follow its own initial trajectory. For small spherical droplets in an incompressible flow, the Stokes number can be recast in terms of the appropriate length scales characteristic of the pore-scale flow,

$$\text{Stk} = \frac{2\rho_d}{9\rho_f} \left(\frac{d_d}{d_p}\right)^2 \text{Re}_p, \tag{13}$$

where ρ_d and ρ_f are the density of the droplet and air phases, respectively, and d_d is the droplet diameter. The Reynolds number, Re_p , is based on the characteristic size of the pore space, d_p . The Stokes number can be plotted as a function of the capture efficiency, ξ , which is defined as

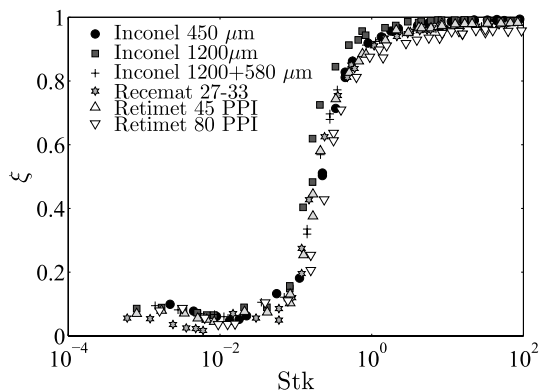
$$\xi = 1 - \eta_{fd}. \quad (14)$$

The oil capture efficiency at $z/d_p = 5$ is plotted in Fig. 11 as a function of the Stokes number of for all samples simulated. There are similarities between the oil separation phenomena described by the pore-scale simulations performed here and particle deposition studies carried out on an array of cylinders (Haugen and Kragset 2010). The Stokes number is taking into account all droplet diameters and flow inlet velocities. The S-shaped capture efficiency curve is typically characteristic of dilute particle flows where the inertial effects are the dominant cause of particle deposition (Konstandopoulos et al. 1993). For Stokes numbers below 0.1, the capture efficiency is quite small and remains rather constant independently of the Stokes number. However, for $0.1 < \text{Stk} < 1$, the oil capture efficiency increases dramatically with increasing Stokes number. Stokes number values above 1 are associated with a very high capture efficiency, which remain stable with increasing Stokes numbers.

The results obtained with the Lagrangian simulations are able to provide a general picture of oil capture effectiveness of the foam samples investigated. However, one should bear in mind the several limitations of the current modelling methodology. According to Haugen and Kragset (2010), the interception of a particle by a solid body, such as a cylinder for example, can be heavily influenced by the boundary layer characteristics next to the solid surface. Therefore, most studies tend to employ very fine levels of discretization next to the solid surface in order to fully resolve the boundary layer (most numerical particle deposition studies deal with simulating a single or several cylinders at most). Here, even though the mesh was refined up to a point where the cells next to the foam surface are located within the viscous sub-layer ($y^+ < 5$), it remains an open question whether this level of refinement was sufficient to accurately resolve all relevant boundary layer flow features.

Additionally, virtually all phenomena related to droplet dynamics were neglected at the present stage. The oil film formation was not allowed to take place upon droplet impact onto the foam surface. Moreover, no splashing, stripping or rebound of droplets was allowed either. The reason for these simplifications are partially due to the lack of an appropriate numerical framework for modelling these phenomena and, even if there were such a framework, the computational cost would be large. However, work continues apace and recent advances by, for example, Kakimpa et al. (2016) on film modelling suggest a framework may be within reach. As mentioned earlier, the simplified mathematical models

Fig. 11 Oil droplet capture efficiency as a function of the Stokes number for all foams analysed at the normalized position $z/d_p = 5$ (with exception of the Retimet 20 PPI)



which are available tend to rely heavily on empirical correlations obtained from idealized test cases, carried out in conditions far different from those present here. As stated in the review by Yarin (2006), there is still a lot of improvements yet to be made in order to have reliable and computationally cost-effective droplet-impact-related models. Nevertheless, the Lagrangian oil capture approach described here offers a first glimpse on modelling the dispersed gas-liquid flow in open-cell metal foams.

3 Modelling at the Macroscopic Scale

One of the main objectives of the present work is to use a pore-scale simulations to extract information otherwise inaccessible when using macroscopic modelling approaches, or for which there is no experimental data available. The results obtained with the pore-scale simulations should be volume-averaged in a way that they can be employed into a macroscopic flow modelling approach, i.e. a formulation that is able to capture the effects caused by the presence of a porous medium on the two-phase flow but that does not explicitly represent the porous geometry.

The pore-scale droplet extinction curves (Fig. 8) obtained by computing the impact location of each droplet along the entire metal foam length can be used in order to derive a function that relates the droplet diameter, flow velocity and capture effectiveness for a given foam sample. For that purpose, the oil capture can be plotted as a function of the normalized streamwise distance travelled by the droplet inside the foam, z/d_p . An exponential function can be fitted to each curve

$$\eta_{fd} = e^{-\beta z}, \quad (15)$$

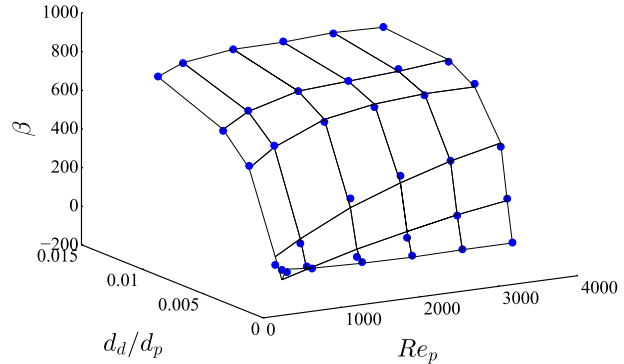
where β is the curve fitting coefficients. The overall quality of the curve fitting is good, and square of the correlation coefficient was always larger than 0.95. The curve fitting procedure is applied for all the oil capture curves obtained by the Lagrangian simulations for a given foam sample, and a value of the coefficient β is obtained for each curve with β being a function of both the droplet diameter and velocity. However, instead of using the droplet diameter and velocity, it is better to use dimensionless quantities. In that sense, β is assumed to be a function of the pore-based Reynolds number, Re_p , and the droplet diameter normalized by the mean pore diameter, d_d/d_p . Thus, β values can subsequently be fitted by a n -order polynomial surface of the form

$$\beta = \sum_{j=0}^n \sum_{k=0}^n a_{j,k} \left(\frac{d_d}{d_p} \right)^j Re_p^k, \quad (16)$$

where $a_{j,k}$ represents the polynomial coefficients. Figure 12 shows the outcome of the surface fitting approach for the oil capture data obtained from the Retimet 45 PPI Lagrangian simulations with a 5th-order polynomial.

The outcome from the surface fitting approach is a function that relates the fraction of free (non-captured) droplets with the distance travelled within the porous region, the normalized droplet diameter and flow pore-based Reynolds number. Although the overall quality of the surface fitting approach is good, the fitted surface tends to produce negative β values at very low d_d/d_p and Re_p values. In the present context, high β values imply higher chances of a droplet being captured, and $\beta = 0$ is the equivalent of a droplet having no chance of being captured. Therefore, negative β are not physical

Fig. 12 Illustration the outcome of the surface fitting approach. Values of β are shown as blue points, and plotted as a function of d_d/d_p and Re_p . The surface is fitted using a fifth order polynomial



and so are assumed to equal zero. For the sake of completeness, this undershoot of β values in the surface fitting could not be avoided even when more data points were used (meaning Lagrangian oil capture results comprising more droplet diameters and flow velocities). Furthermore, changing the order of the surface polynomial did not prevent this undershoot either.

3.1 Macroscopic Droplet Capture UDF

In de Carvalho et al. (2016) it was briefly mentioned that a macroscopic particle capture model was in development. Here, the fruits of that development work are presented. An user-defined function (UDF) was written in order to implement this oil capture function in ANSYS Fluent. At each Lagrangian calculation step, each droplet parcel will have a certain probability of being captured, depending on the distance travelled inside the porous medium, the droplet diameter and its velocity. Therefore, the UDF works by tracking the droplets that are travelling inside the porous region, and randomly terminating their trajectory according to a probability that is computed based on the outcome of the surface fitting approach.

The capture of the droplets as they pass through the porous region is achieved in an analogous way to the modelling of radioactive decay. Here, rather considering the probability that a nuclei will decay in a given time, we have the probability, $P(z)$, that a droplet can travel some distance, z , through the porous medium without it being captured

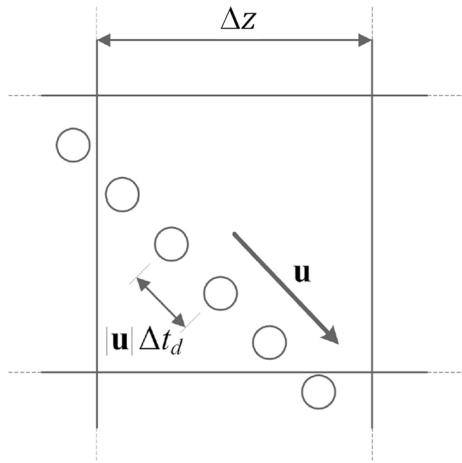
$$P(z) = \exp(-\beta z), \quad (17)$$

where β is the equal to β in Eq. 15. So, when $z = 0$, it is certain to not have been captured, as $z \rightarrow \infty$, then it is certain to have been captured.

In Fluent, each particle that is being tracked steps forward in space in a number of increments, governed by the particle timestep Δt_d . This is not to be confused with the flow timestep for transient simulations, which can be completely different. Depending on the mode of operation, the code works out the size of the particle timestep based on the velocity in, \mathbf{u} , and size of, Δz , the cell which the particle is in (Fig. 13). It then tries to ensure that the particle will take n steps through the cell, where n is typically 5.

As the droplet/particle moves through the cell, the UDF that was written for the purpose, calculates the distance the particle moves in a timestep, $\mathbf{u}\Delta t_d$. A random number generator then produces a number, λ_{01} , between 0 and 1. If $\lambda_{01} < \beta\mathbf{u}\Delta t_d$, then the droplet is

Fig. 13 Schematic of the transit of a droplet through a mesh cell in Fluent



deemed to have been captured and the mass of the droplet is stored in a user-defined memory (UDM), which keeps a tally of the mass of droplet(s) captured in that mesh cell. When captured, the droplet is removed from the droplets being tracked and ceases to exist. Rather than explicitly calculate $\mathbf{u}\Delta t_d$, the UDF finds the difference between the droplet's coordinates from the previous and current particle timestep, leaving the calculation of these positions to the particle tracking algorithm.

To calculate β at each particle timestep, the pore-based Reynolds number, Re_p , and the normalised droplet diameter, d_d/d_p , are calculated and β is found from Eq. 16.

The key aspect of this approach is that it is stochastic and treats every particle timestep as distinct and independent. There is no cumulative effect implicit in this method, the droplet “has no memory” that it may have travelled some distance through the porous medium already. In many ways, it mimics the real experience of the droplet, where at each instant there is a chance that it may encounter a filament inside the metal foam, something that is not influenced from whence it came.

3.2 Verification of the Macroscopic Droplet Capture Model

A simple test case was devised in order to validate the enhanced macroscopic porous model described here. The validation is done by comparing the results of the macroscopic model simulations against pore-scale results. Thus, a computational domain with the same dimensions as the pore-scale domain employed for the Retimet 45 PPI simulations is created. Figure 14 illustrates the computational domain of the macroscopic model validation case. The dimensions are exactly the same as for the square channel domain employed in the Retimet 45 PPI pore-scale simulations. The main difference is that instead of explicitly representing the metal foam, a porous region is defined instead. A hexahedral mesh was employed with a total mesh count of 10 000 cells. For comparison purposes, the pore-scale domain for the Retimet 45 PPI had 4.72×10^6 mesh cells. In essence, the intricate structure of a pore within the pore-scale CFD model (represented by 10s of thousands of polyhedral cells) is replaced by several hexahedral cells in the macroscopic CFD model—they are simply cells in the macroscopic model where the porous media model is applied.

The boundary conditions are exactly the same as the ones used in the pore-scale simulations, except for the porous region. Viscous and inertial resistance coefficients were defined

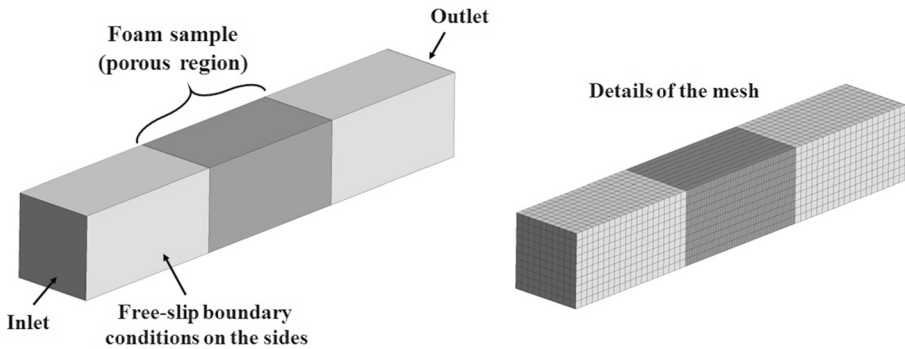


Fig. 14 Illustration the computational domain used for validation of the macroscopic porous media model. Domain dimensions are identical to the pore-scale square channel domain employed for the Retimet 45 PPI simulations. A porous region is defined instead of explicitly representing the Retimet 45 PPI porous geometry

for the porous region using the values of permeability and Forchheimer coefficient computed from the pore-scale simulations results for the Retimet 45 PPI. Simulations are carried out for incompressible steady-state airflow using the RNG k - ϵ turbulence model for a velocity range of 5–50 m/s.

Figure 15 depicts the static pressure contour plots for both approaches—in each case the pressure drop is confined to the foam. In the case of the pore-scale simulations, a complex pressure distribution is seen due to the complex foam geometry, whereas a linear pressure drop is observed for the macroscopic case. Quantitatively, there is good agreement for the pressure drop (presented as a percentage of the maximum pressure drop seen across the simulations) for different inlet velocities in both cases (Fig. 16). Here we see the characteristic relationship between the pressure drop and the square of the inlet velocity as can be expected from Eq. 1 when the Forchheimer coefficient, F , dominates, as is the case for these metal foams (de Carvalho et al. 2017). Lagrangian oil droplet tracking calculations are performed using the same settings as the ones used for the pore-scale simulations. For that purpose, the droplets are injected in a plane located halfway between the inlet and the entrance to the porous region. The UDF described in Sect. 3.1 randomly terminated the droplet trajectories. Therefore, for verification purposes, droplet capture curves were extracted in exactly the same way as for the pore-scale simulations. The termination of droplet trajectories due to the macroscopic oil capture model is clearly shown in Fig. 17, which shows a the trajectories across the macroscopic Retimet 45 PPI foam model at an inlet velocity of 20 m/s and two uniform droplet diameters: 1 and 3 μm . In the same sense as for the pore-scale Lagrangian simulations, as the droplet diameter increases, so does the probability of it being captured, or in the context of the UDF, having its trajectory terminated.

While Fig. 17 is appealing, a more quantitative comparison between the pore-scale and macroscopic models is required. The fraction of free droplets for both approaches is computed at the normalized position $z/d_p = 5$, and plotted for both approaches in Fig. 18 for four different droplet diameters at varying flow velocities. The results obtained with the macroscopic oil extinction model showed a good

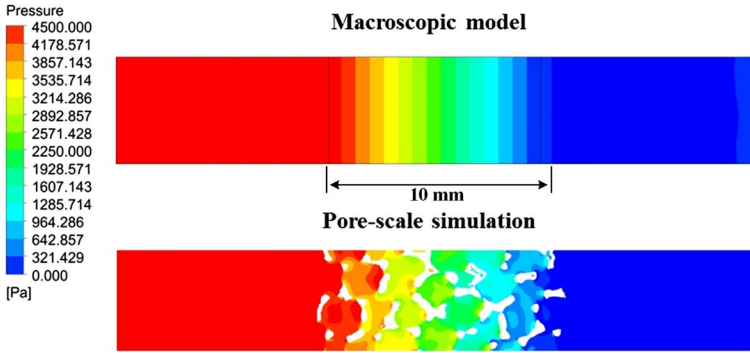
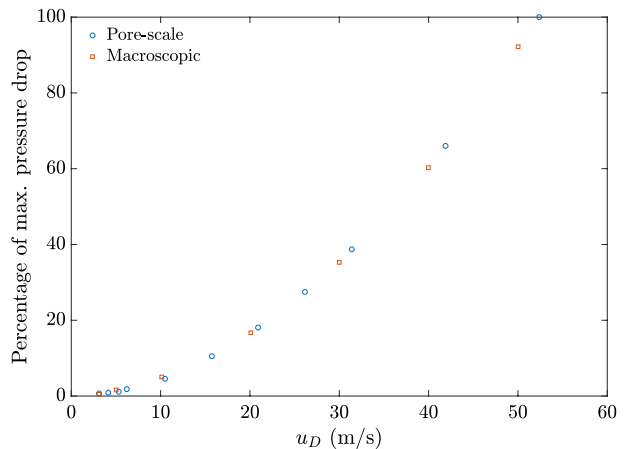


Fig. 15 Comparison of the static pressure contour plots obtained by the pore-scale and macroscopic model simulations for the Retimet 45 PPI foam, at $u_D = 20\text{m/s}$

agreement with the pore-scale results. Larger deviations from the pore-scale results are observed for a droplet diameter of $0.5\ \mu\text{m}$, at lower flow velocities. This was expected, as the surface fitting procedure described previously produces negative β values within a small region which is representation of small droplet sizes and low flow velocities.

Figure 19 depicts the droplet capture curves computed from the pore-scale and macroscopic simulations, respectively. The results show the fraction of free droplets as a function of the normalized streamwise foam length at a flow velocity of 20 m/s , for four droplet diameters $0.5, 1, 3$ and $5\ \mu\text{m}$. The results obtained for the other foams showed very similar trends. For all the foams, the worst agreement between both approaches occurs for the smallest droplets sizes. However, this is really due to the polynomial surface fitting, which we reiterate does not work well for the smallest diameter droplets and lowest inlet velocities.

Fig. 16 Comparison of the pressure drop obtained by the pore-scale and macroscopic model simulations for the Retimet 45 PPI foam



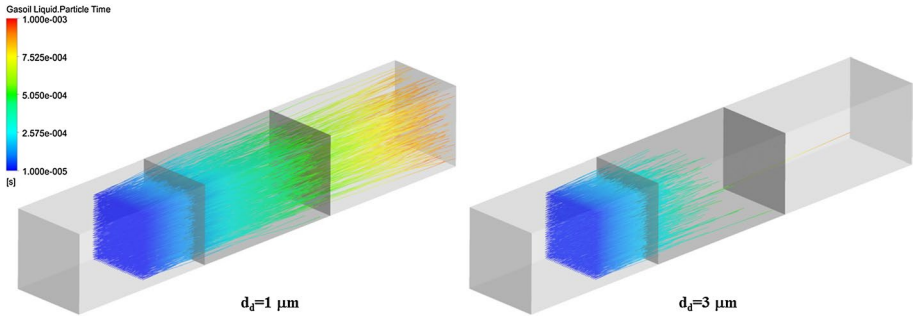


Fig. 17 Droplet trajectories through the macroscopic Retimet 45 PPI foam model for an inlet velocity of 20 m/s and two uniform droplet diameters: 1 and 3 μm . The number of trajectories was reduced for clarity

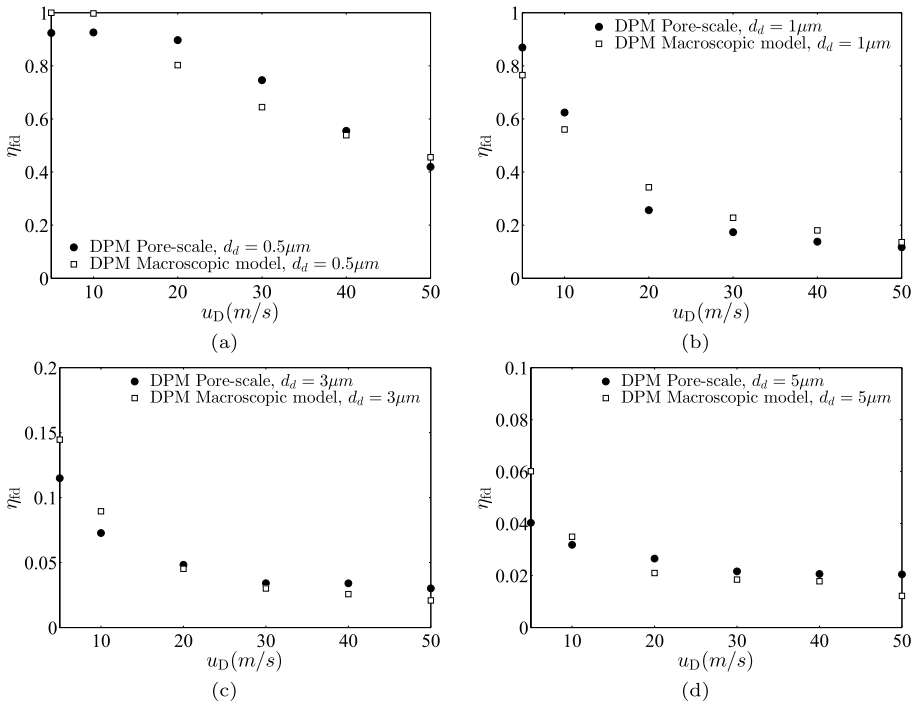


Fig. 18 Comparison between the results obtained by the pore-scale and macroscopic model Lagrangian calculations showing the fraction of non-captured droplets computed at the normalized position $z/d_p = 5$ versus the Darcian velocity for four different droplet diameters **a** 0.5, **b** 1, **c** 3 and **d** 5 μm

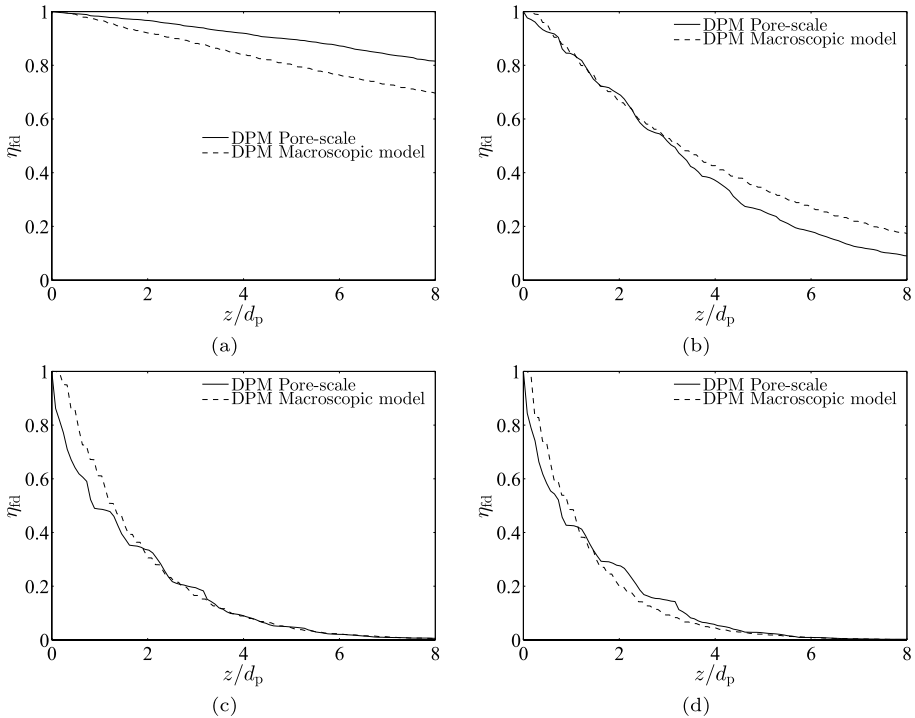


Fig. 19 Comparison between the results obtained by the pore-scale and macroscopic model Lagrangian calculations showing the oil capture curves computed from the pore-scale and macroscopic model calculations, respectively. Results are shown for four droplet diameters **a** 0.5, **b** 1, **c** 3 and **d** 5 μm at a Darcian velocity of 20 m/s

4 Conclusions

The methodology for a new approach to the macroscopic modelling of droplet capture in porous media is presented in this paper. While the pore-scale determination of both the permeability and the Forchheimer coefficients has been routinely transferred into macroscopic models, this is the first time pore-scale droplet capture has been treated in a similar manner. This approach means that a limited number of high-resolution, pore-scale CFD models can be conducted to determine the droplet capture coefficient, β , for a particular porous medium (in this case open-cell metal foams) and then this can be transferred to a low-resolution macroscopic model. This will be advantageous when the porous region forms only a small portion of a much larger piece of machinery and is standard practice in the CFD industry, at least for the hydrodynamic effects of the porous region. This extension to include droplet capture using a stochastic method opens up new application areas.

While the verification exercise presented here confirms the equivalence of the pore-scale and macroscopic approaches, there is still a need for validation against actual experiments and these will be the focus of future work. However, the basis of the model is, we feel, firm and will prove useful in these subsequent studies.

The surface fitting approach employed here seems to have a reduced accuracy for the oil capture results obtained at low flow velocities and for smaller droplet diameters.

Nevertheless, the main objective of the present work is to provide a qualitative evaluation of the oil capture effectiveness in several commercial open-cell metal foams. Given the fact that the pore-scale Lagrangian oil capture results already take into account a certain degree of uncertainty, it is reasonable to say that the macroscopic oil capture model described here still provides a good qualitative agreement of the droplet extinction rates throughout the foam samples. Furthermore, the enhanced macroscopic model can be easily implemented in a commercial CFD solver, with very low associated computational costs.

Author Contributions Conceptualization was contributed by TC, DH, HM and MK; Methodology was contributed by TC, DH and HM; Formal analysis and investigation were contributed by TC; Writing—original draft preparation was contributed by TC and DH; Writing—review and editing was contributed by TC, DH, HM and MK; Funding acquisition was contributed by HM and MK; Resources were contributed by HM; Supervision was contributed by HM and DH.

Funding The research leading to these results has received funding from the European Union Seventh Framework Programme under Grant agreement Number 314366 (E-BREAK project). In addition, the authors would like to acknowledge the use of the High Performance Computer at the University of Nottingham.

Data availability The datasets generated during and/or analysed during the current study are not publicly available.

Declarations

Conflict of interest The authors have no relevant financial or non-financial interests to disclose.

Open Access This article is licensed under a Creative Commons Attribution 4.0 International License, which permits use, sharing, adaptation, distribution and reproduction in any medium or format, as long as you give appropriate credit to the original author(s) and the source, provide a link to the Creative Commons licence, and indicate if changes were made. The images or other third party material in this article are included in the article's Creative Commons licence, unless indicated otherwise in a credit line to the material. If material is not included in the article's Creative Commons licence and your intended use is not permitted by statutory regulation or exceeds the permitted use, you will need to obtain permission directly from the copyright holder. To view a copy of this licence, visit <http://creativecommons.org/licenses/by/4.0/>.

References

- Banhart, J.: Manufacture, characterisation and application of cellular metals and metal foams. *Prog. Mater Sci.* **46**(6), 559–632 (2001)
- de Carvalho, T., Morvan, H., Hargreaves, D., Cordes, L., Hofler, C.: Limitations of a state-of-the-art numerical modelling framework for two-phase flow in aero-engine air/oil separators. *ASME Turbo Expo 2016: Turbomachinery Technical Conference and Exposition* (2016)
- de Carvalho, T., Morvan, H., Hargreaves, D., Oun, H., Kennedy, A.: Experimental and tomography-based CFD investigations of the flow in open cell metal foams with application to aero engine separators. *ASME Turbo Expo 2015: Turbine Technical Conference and Exposition* (2015)
- de Carvalho, T., Morvan, H., Hargreaves, D., Oun, H., Kennedy, A.: Pore-scale numerical investigation of pressure drop behaviour across open-cell metal foams. *Transp. Porous Media* **117**(2), 311–336 (2017)
- Dukhan, N., Bağcı, Ö., Özdemir, M.: Metal foam hydrodynamics: flow regimes from pre-darcy to turbulent. *Int. J. Heat Mass Transf.* **77**, 114–123 (2014)
- Eaton, J.: Two-way coupled turbulence simulations of gas-particle flows using point-particle tracking. *Int. J. Multiph. Flow* **35**(9), 792–800 (2009)
- Elghobashi, S.: On predicting particle-laden turbulent flows. *Appl. Sci. Res.* **52**(4), 309–329 (1994)
- Gerbaux, O., Buyens, F., Mourzenko, V., Memponteil, A., Vabre, A., Thovert, J.-F., Adler, P.: Transport properties of real metallic foams. *J. Colloid Interface Sci.* **342**(1), 155–165 (2010)

- Haugen, N., Kragset, S.: Particle impaction on a cylinder in a crossflow as function of Stokes and Reynolds numbers. *J. Fluid Mech.* **661**, 239–261 (2010)
- Hirt, C.W., Nichols, B.D.: Volume of fluid (VOF) method for the dynamics of free boundaries. *J. Comput. Phys.* **39**(1), 201–225 (1981)
- Hosseini, S., Vahedi Tafreshi, H.: 3-D simulation of particle filtration in electrospun nanofibrous filters. *Powder Technol.* **201**, 153–160 (2010)
- Hosseini, S., Vahedi Tafreshi, H.: Modeling particle filtration in disordered 2-D domains: a comparison with cell models. *Sep. Purif. Technol.* **74**, 160–169 (2010)
- Ji, K., Zhang, J., Chen, J., Meng, G., Ding, Y., Dai, Z.: Centrifugation-assisted fog-collecting abilities of metal-foam structures with different surface wettabilities. *ACS Appl. Mater. Interfaces* **8**(15), 10005–10013 (2016)
- Kakimpa, B., Morvan, H., Hibberd, S.: The depth-averaged numerical simulation of laminar thin-film flows with capillary waves. *J. Eng. Gas Turbines Power* **138**, 112501 (2016)
- Konstandopoulos, A., Labowsky, M., Rosner, D.: Inertial deposition of particles from potential flows past cylinder arrays. *J. Aerosol Sci.* **24**(4), 471–483 (1993)
- Kulick, J., Fessler, J., Eaton, J.: Particle response and turbulence modification in fully developed channel flow. *J. Fluid Mech.* **277**, 109–134 (1994)
- Morsi, S., Alexander, A.: An investigation of particle trajectories in two-phase flow systems. *J. Fluid Mech.* **55**(02), 193–208 (1972)
- Nie, Z., Lin, Y., Tong, Q.: Numerical simulations of two-phase flow in open-cell metal foams with application to aero-engine separators. *Int. J. Heat Mass Transf.* **127**, 917–932 (2018)
- Oun, H., Kennedy, A.: Experimental investigation of pressure-drop characteristics across multi-layer porous metal structures. *J. Porous Mater.* **21**(6), 1133–1141 (2014)
- Peduto, D., Koch, R., Morvan, H., Dullenkopf, K., Bauer, H.: Numerical studies of single drop impact onto a plane shallow an deep liquid pool. In: *Proc. of 24th European Conference on Liquid Atomization and Spray Systems* (2011)
- Willenborg, K., Klingsporn, M., Tebby, S., Ratcliffe, T., Gorse, P., Dullenkopf, K., Wittig, S.: Experimental analysis of air/ oil separator performance. *J. Eng. Gas Turbines Power* **130**(6), 062503 (2008)
- Yarin, A.: Drop impact dynamics: splashing, spreading, receding, bouncing. *Annu. Rev. Fluid Mech.* **38**, 159–192 (2006)

Publisher's Note Springer Nature remains neutral with regard to jurisdictional claims in published maps and institutional affiliations.